Dynamical Links between the Decadal Variability of the Oyashio and Kuroshio Extensions

BO QIU, SHUIMING CHEN, AND NIKLAS SCHNEIDER

Department of Oceanography, University of Hawai'i at Mānoa, Honolulu, Hawaii

(Manuscript received 9 June 2017, in final form 29 August 2017)

ABSTRACT

Rather than a single and continuous boundary current outflow, long-term satellite observations reveal that the Oyashio Extension (OE) in the North Pacific Subarctic Gyre comprises two independent, northeast–southwest-slanted front systems. With a mean latitude along 40°N, the western OE front exists primarily west of 153°E and is a continuation of the subarctic gyre western boundary current. The eastern OE front, also appearing along 40°N, is located between 153° and 170°E, whose entity is disconnected from its western counterpart. During 1982–2016, both of the OE fronts exhibit prominent decadal fluctuations, although their signals show little contemporaneous correlation. An upper-ocean temperature budget analysis based on the Estimating the Circulation and Climate of the Ocean, phase II (ECCO2), state estimate reveals that the advective temperature flux convergence plays a critical role in determining the low-frequency temperature changes relating to the OE fronts. Specifically, the western OE front variability is controlled by the decadal mesoscale eddy modulations in the upstream Kuroshio Extension (KE). An enhanced eddy activity increases the poleward heat transport and works to strengthen the western OE front. The eastern OE front variability, on the other hand, is dictated by both the meridional shift of the KE position and the circulation intensity change immediately north of the eastern OE. Different baroclinic adjustment speeds for the KE and OE are found to cause the in-phase changes between these latter two processes. Lack of contemporaneous correlation between the decadal western and eastern OE variability is found to be related to the interaction of the meridionally migrating KE jet with the Shatsky Rise near 159°E.

1. Introduction

The western boundary current (WBC) system in the midlatitude North Pacific is unique in the sense that the Kuroshio and Oyashio Extensions of the wind-driven subtropical and subpolar gyres flow approximately parallel east of Japan over a distance greater than 3000 km [comprehensive reviews of these two WBC extensions can be found in Qiu (2001), Yasuda (2003), and Kida et al. (2015)]. Despite their proximity over such a long distance, studies of the low-frequency variability of the Kuroshio and Oyashio Extensions have largely proceeded independently in the past because these two WBC extensions possess very different dynamical properties.

Being an intense baroclinic inertial jet, the Kuroshio Extension (KE) variability is reflected strongly in the time-varying sea surface height (SSH) field, making it easy to be detected and examined by satellite altimetry measurements. Figure 1a shows the mean SSH map in the northwestern Pacific Ocean wherein the eastward-flowing KE can be clearly identified by the sharp SSH gradient aligned approximately along 35°N. Reflecting its unstable nature, most of the eddying surface velocity signals are concentrated along the path of the KE jet (Fig. 1b). Based on the long-term satellite altimeter measurements, a significant advancement has been made over the last two decades regarding the phenomenology and dynamic causes for the low-frequency KE changes. Indeed, a rich literature is available now indicating that the KE exhibits well-defined decadal modulations between a stable and an unstable dynamic state (e.g., Qiu and Chen 2005, 2010; Taguchi et al. 2007; Qiu et al. 2007; Sugimoto and Hanawa 2009; Ceballos et al. 2009; Kelly et al. 2010; Sasaki et al. 2013; Sugimoto et al. 2014; among others). When in its stable dynamic state, the KE has been observed to have an intensified eastward transport, a northward latitudinal position, an enhanced southern recirculation gyre, and a decreased regional eddy kinetic energy level. The reverse is true when the KE switches to an unstable dynamic state.

In comparison, the Oyashio Extension (OE) possesses few SSH expressions as a result of strong density compensation between the temperature and salinity variations

Corresponding author: Dr. Bo Qiu, bo@soest.hawaii.edu

DOI: 10.1175/JCLI-D-17-0397.1

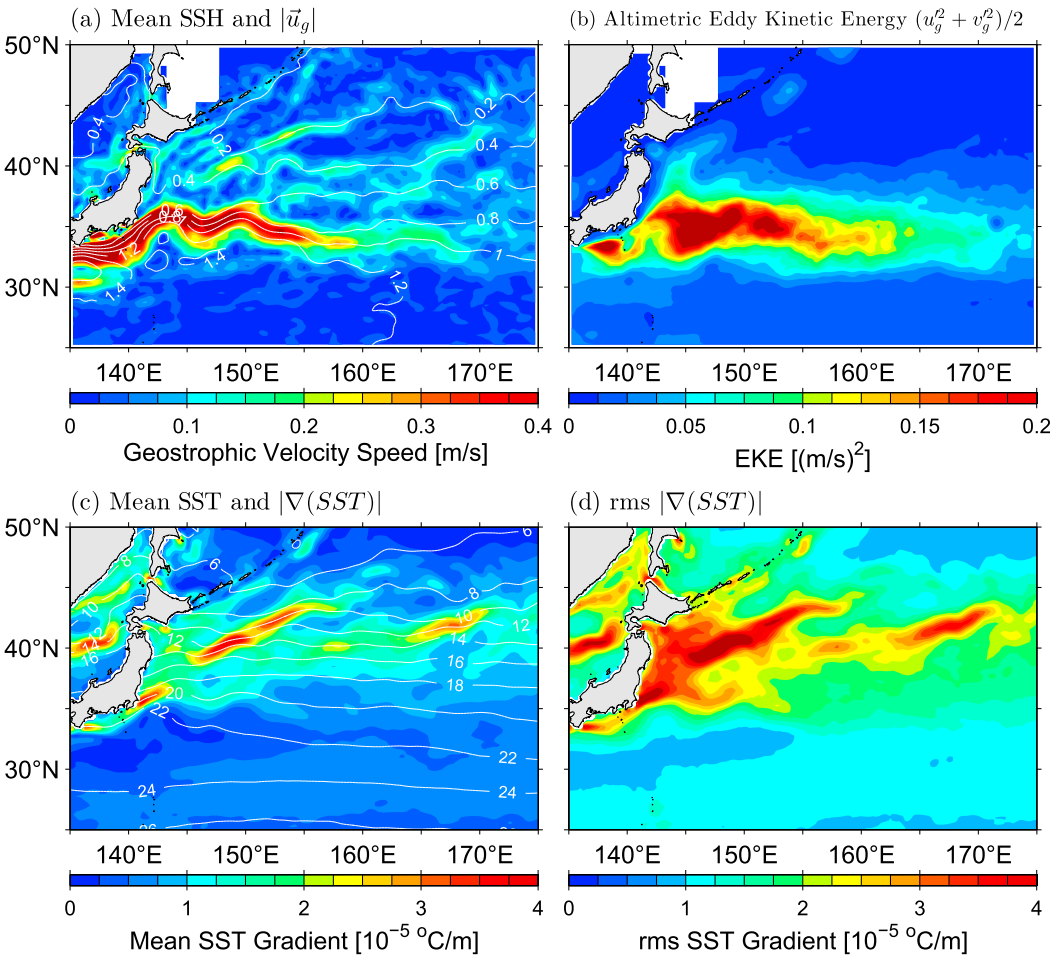

FIG. 1. (a) Mean SSH field (m; white contours) surrounding the KE–OE region from Rio et al. (2011). Color shading indicates the corresponding speed of the mean surface geostrophic flows. (b) Surface eddy kinetic energy map calculated from the AVISO SSH anomalies of 1993–2016. (c) Mean SST field (°C; white contours) surrounding the Kuroshio and Oyoshio Extension region from Reynolds et al. (2007) during 1982–2016. Color shading indicates the magnitude of the horizontal SST gradient during the same period. (d) Root-mean-square amplitude of the time-varying SST gradient during 1982–2016.

(e.g., Yuan and Talley 1996). While weak in SSH expressions, the OE is accompanied by intense sea surface temperature (SST) and salinity fronts. Rather than a single and spatially contiguous front and eastward current, Fig. 1c indicates that the OE along the latitude band of 38°–43°N comprises two quasi-permanent and northeast–southwest-oriented SST fronts. The western OE front (OE-west) appears between 145° and 153°E and is a continuation of the wind-driven Oyashio that flows southward along the Kuril Islands and Hokkaido (Kawai 1972). The eastern OE front (OE-east) exists between 153° and 173°E and is sometimes referred to as the Subarctic Boundary (SAB; e.g., Favorite et al. 1976). Notice that though weak in intensity, these two northeast–southwest-oriented OE SST fronts are accompanied by the locally enhanced, time-mean surface flows as discernible in Fig. 1a. Such time-mean flow features have been previously noted by Isoguchi et al. (2006) in their study of the surface OE.

A look at the SST gradient variance map in the region (Fig. 1d) reveals that the two OE fronts have their respective, locally enhanced variations. An empirical orthogonal function (EOF) analysis focusing on the nonseasonal maximum SST gradients in the western versus eastern OE regions (i.e., 141°–153°E vs 153°–173°E) indicates that the two OE fronts exhibit different interannual and longer time-scale variations (Fig. 2).[1] In fact, the linear correlation between the principal component (PC) of the first EOF modes associated with the western and eastern OE fronts

[1] Our EOF analysis follows that conducted by Frankignoul et al. (2011), and its details are provided in section 3.

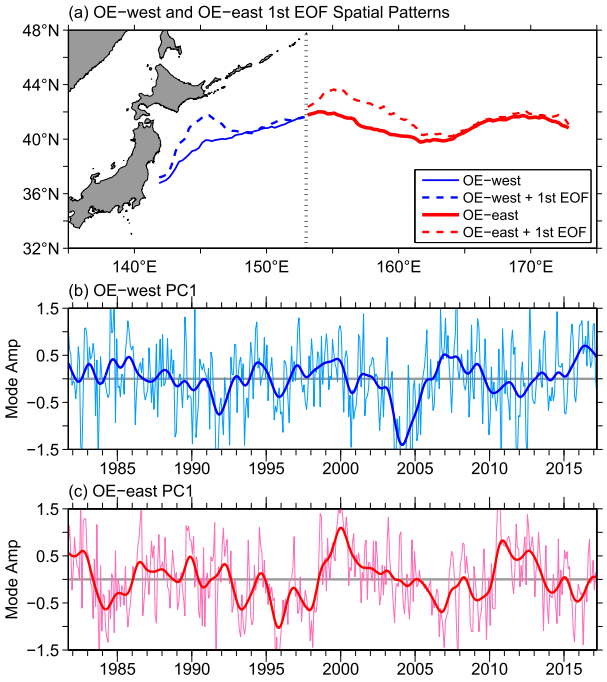

FIG. 2. (a) Mean latitude position of maximum meridional SST gradient of OE west vs east of 153°E (blue vs red lines). Dashed blue and red lines denote the spatial structures of the first EOF mode west vs east of 153°E. (b) PC of the first EOF mode west of 153°E. Thin line denotes the monthly time series, and thick line denotes the time series after a Gaussian low-pass filtering that has half-power at 4 months. (c) As in (b), but for east of 153°E.

is −0.09 (cf. Figs. 2b and 2c, respectively). As such, distinction is needed in exploring the OE variability between its western versus eastern SST fronts.

Owing to its broader extension in parallel to the overlying storm tracks of the extratropical North Pacific (Nakamura et al. 2004), the eastern OE front has been the main focus in previous studies of the OE variability in connection to the midlatitude ocean–atmosphere interaction. Indeed, the mode-1 PC time series shown in Fig. 2c reproduces the OE index introduced by Frankignoul et al. (2011, hereafter FSKA11) to capture the low-frequency OE-east variability. Through maintaining the lower-tropospheric baroclinicity and anchoring the extratropical storm tracks, changes in the OE-east have been demonstrated by many investigators to affect the Pacific-basin time-mean and time-varying atmospheric circulation (e.g., Nakamura et al. 2008; Taguchi et al. 2009, 2012; Kwon et al. 2010; FSKA11; Kwon and Joyce 2013; O'Reilly and Czaja 2015; Smirnov et al. 2015; Masunaga et al. 2016; Ma et al. 2016; Révelard et al. 2016).

In comparison to the extensive exploration of the impact of OE variability upon the overlying atmosphere, our understanding about the causes that generate the OE variability remains limited. Using both ship and satellite SST measurements of 1982–96, Nakamura and Kazmin (2003) detected a decadal intensification of the OE front during the period of 1988–94. They attributed this frontal intensification to the combined surface net heat flux and Ekman flux convergence forcing. Based on lead–lag regression analysis, Nonaka et al. (2008) found that the Oyashio variability west of 152.5°E (i.e., the western OE front defined above) is generated by basin-scale wind stress curl and local Ekman pumping forcings via both baroclinic and barotropic Rossby wave propagations. The importance of the basin-scale wind forcing in shifting the OE front has also been emphasized previously by Seager et al. (2001), Schneider et al. (2002), Nonaka et al. (2006), and Kwon and Deser (2007). More recently, with the use of output from a 35-yr ocean general circulation model (OGCM) simulation, Pak et al. (2017) examined the upper-ocean temperature variations in the KE–OE confluence region of 36°–42°N, 150°–165°E. They emphasized the importance of temperature advective fluxes in controlling the rate of temperature change and related the anomalous advective fluxes to the meridional shift of the OE front.

Because of the nonlinear nature of oceanic western boundary currents, an unconstrained OGCM forced by observed surface heat fluxes is not guaranteed to produce the observed SST and upper-ocean temperature content changes. For example, a recent study by Yang et al. (2017) shows that the global OGCM for the Earth Simulator (OFES) simulation, which has an eddy-resolving $^1/_{10}°$ horizontal grid resolution, fails to capture the observed decadal modulations of mesoscale eddies in the KE–OE region, despite the fact that OFES reproduces well the large-scale KE variability on decadal time scales (Taguchi et al. 2007). Given the well-documented importance of mesoscale eddies in contributing to the mixed layer evolution and upper-ocean thermal structures in the KE and OE regions (e.g., Qiu and Chen 2006; Sugimoto and Hanawa 2011; Kouketsu et al. 2012; Oka et al. 2012), it is imperative to utilize a dynamically and thermodynamically consistent model output to elucidate the processes underlying the low-frequency changes of the OE fronts.

To meet this requirement, we use in this study the ocean state estimate from the Estimating the Circulation and Climate of the Ocean, phase II (ECCO2). Since it is constructed in a dynamically and thermodynamically consistent way (see section 2) and produces favorably the mesoscale eddy modulations observed in the KE–OE region (Yang et al. 2017), the ECCO2 state estimate is uniquely suited to quantify the differing processes governing the western versus eastern OE front variations as shown in Figs. 2b,c.

This paper is organized as follows. In section 2, we provide a brief description about the ECCO2 state estimate and other observational datasets used in this

study. In section 3, the low-frequency OE variability is examined and its connections to the KE variability are explored. Section 4 investigates the processes that control the low-frequency variability of the OE fronts; differences between the western versus eastern OE front are contrasted. In section 5, we discuss the analysis results and attempt to establish a unified framework for understanding the interlinked KE and OE variability. A summary of the present study is given in section 6.

2. ECCO2 state estimate and observational data

The ECCO2 model is based on the Massachusetts Institute of Technology General Circulation Model (MITgcm; Marshall et al. 1997), a three-dimensional, z-level, hydrostatic and Boussinesq global ocean model. It uses a cubed-sphere grid projection (cube92 version) with a mean horizontal resolution of 18 km. In the vertical, the model has 50 levels, with resolution varying from 10 m near the sea surface to 456 m near the ocean bottom at a maximum depth of 6150 m. The eddy-permitting ocean state estimate is obtained by a least squares fit of the MITgcm to available satellite and in situ data. Using a Green's function approach (Menemenlis et al. 2005), the least squares fit is employed for a number of control parameters of the model: the initial temperature–salinity conditions, surface boundary conditions, background eddy viscosity and diffusivity, and bottom drag. Using the optimized control parameters, the model is run forward unconstrained as in other prognostic model simulations. Since no observational data are inserted in the forward integration, the ECCO2 state estimate is regarded to be dynamically and thermodynamically consistent (Wunsch et al. 2009). The ECCO2 state estimate has been used in the past to diagnose the eddy–mean flow interaction energetics in different parts of the world oceans (e.g., Fu 2009; Chen et al. 2014; Yang et al. 2017). For this study, we use the 3-day-averaged output of the ECCO2 state estimate from 1992 to 2016.

Two observational datasets are used in this study to complement the ECCO2 state estimate analysis in the region of our interest. For the SST data, we utilize the high-resolution product of Reynolds et al. (2007) that blended the Advanced Very High Resolution Radiometer (AVHRR) infrared satellite SST data, the Advanced Microwave Scanning Radiometer (AMSR) satellite SST data, and in situ temperature data from ships and buoy measurements. The optimally interpolated SST dataset has a spatial grid resolution of 0.25° and a temporal resolution of 1 day and covers the period from September 1981 to December 2016. Notice that this same SST dataset was previously used by FSKA11 in their analysis of the OE variability.

To examine the surface circulation changes, we use the global SSH anomaly dataset compiled by the Space Oceanographic Division of Collecte Localisation Satellites (CLS), Toulouse, France. This dataset merges along-track SSH measurements from all satellite altimeter missions after October 1992 and has a 7-day temporal resolution and a ¼°-longitude Mercator spatial resolution (Ducet et al. 2000). The data period available for this study extends from January 1993 to December 2016.

3. Low-frequency Oyashio and Kuroshio Extension variability

An effective way to extract the low-frequency OE variations is that of FSKA11, who conducted an EOF analysis on the nonseasonal maximum meridional SST gradient (dSST/dy) anomalies associated with the OE SST front as a function of longitude and time. Here, nonseasonal SST anomalies are defined as the SST deviations from the monthly climatology of 1981–2016. In their analysis, FSKA11 selected the longitudinal band of 145°–170°E and found that the action center of the first dSST/dy EOF mode is between 153° and 165°E (see Fig. 3a in FSKA11). To explore the OE variability more comprehensively, we adopt in this study the same approach but choose to perform the EOF analysis by separating the SST gradient signals into the western and eastern regions delineated by 153°E. This separation makes dynamical sense because, as we reviewed in the introduction, the OE west of 153°E is a direct continuation of Oyashio, the western boundary current of the wind-driven North Pacific Subarctic Gyre. In contrast, the OE SST front east of 153°E has influences from both the KE's quasi-stationary meanders from the southwest and the subarctic circulation from the northwest (cf. Figs. 1a and 1c; Isoguchi et al. 2006).

As shown in Fig. 2a, the action center of the leading mode OE-west variability is centered near 145°E just offshore east of Japan and the mode explains 22.0% of the total variance. Because of the high mesoscale eddy variability to the south of the OE-west front (recall Fig. 1b), the mode-1 PC of the OE-west variability (the thin blue line in Fig. 2b) exhibits large-amplitude intraseasonal fluctuations. Meanwhile, as indicated by the thick blue line, low-frequency modulations are also apparent in Fig. 2b. It is of interest to note that the low-frequency OE-west variability has a close connection to decadally modulated eddy fluctuations in the upstream KE region. Figure 3a shows the time series of the KE pathlength integrated from 141° to 153°E. Here, a large value indicates a convoluted and unstable state of the upstream KE (see, e.g., Fig. 3 in Qiu and Chen 2005). A lead–lag correlation analysis[2]

[2] Unless indicated otherwise, all correlation analyses conducted below are based on the low-pass-filtered time series. The correlation's statistical significance level is based on the degree of freedom estimated from the time series's decorrelation scale.

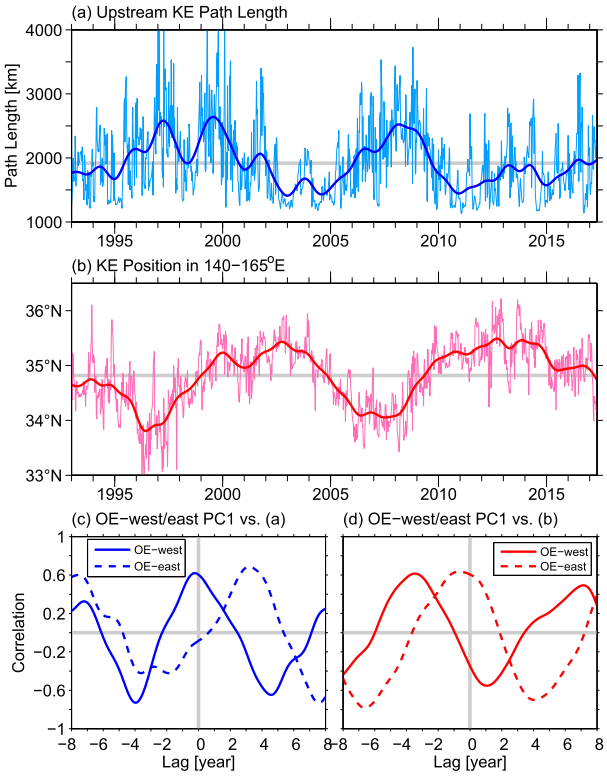

FIG. 3. Time series of (a) the upstream KE pathlength integrated from 141° to 153°E and (b) mean latitudinal KE position averaged from 140° to 165°E. Details about these time series constructions can be found in Qiu and Chen (2005). (c) Lead–lag correlation between the time series shown in (a) and the PC1 time series of Figs. 2b,c. (d) Lead–lag correlation between the time series shown in (b) and the PC1 time series of Figs. 2b,c. In (c) and (d), positive lags indicate the lead by either the time series of (a) or (b).

between Figs. 3a and 2b indicates that the two time series during their overlapping period have an in-phase correlation coefficient $r = 0.60$ (the solid line in Fig. 3c), which is statistically significant at the 95% confidence level. Conceptually, this correlation is easy to comprehend: when the upstream KE becomes unstable with enhanced mesoscale eddy activity, more subtropical-origin warm water is transported northward, resulting in intensification of OE-west offshore of Japan (e.g., Sugimoto et al. 2014; Masunaga et al. 2016). Notice that the upstream KE eddy variability has no concurrent correlation with the eastern OE front variability identified in Fig. 2c (see dashed line in Fig. 3c). The two time series are, however, correlated at a lag of 2.5–3 yr, and the reason for this will become evident in section 5.

East of 153°E, our EOF leading mode results for the OE-east variability are in good agreement to those obtained by FSKA11 both in terms of mode's spatial pattern and temporal fluctuations (cf. Figs. 2a,c with Fig. 3 in FSKA11). Similar to the analysis in FSKA11, this mode explains 14.7% of the total variance. It is interesting to note that the OE-east variability has little concurrent connection to the variations detected in the OE-west region: the contemporaneous correlation between the time series in Figs. 2b,c is only $r = -0.09$. As may be inferred from Fig. 3c, however, the two time series are correlated at $r = 0.44$ with a lag of approximately 3 yr by the OE-east signals.

To relate the OE-east variability to that of the KE, we plot in Fig. 3b the time series of the latitudinal KE position averaged from 140° to 165°E. (Notice that the low-frequency KE position change is zonally coherent; a time series similar to that of Fig. 3b can be obtained if the average is taken from 153° to 165°E.) As indicated by the dashed line in Fig. 3d, the mode-1 PC of OE-east exhibits a favorable, near-in-phase correlation ($r = 0.61$) with the KE position changes. For the OE-west variability, on the other hand, the low-frequency KE position changes show no positive correlations with any lead less than 3 yr (see the solid line in Fig. 3d). Compared with the OE variability west of 153°E, explanation for this connection between the KE position and OE-east variations is less straightforward because it involves not only the KE position variability, but also that of the western subarctic gyre circulation. We will return to examine this connection in section 5 after conducting the upper-ocean temperature budget analysis in the next section.

4. Upper-ocean temperature budget analysis

We have used in the preceding section the meridionally varying maximum $d\mathrm{SST}/dy$ as a measure for identifying the low-frequency OE front fluctuations. This measure, however, is not exclusive and represents only one manifestation of the low-frequency OE front fluctuations. Western and eastern OE-index time series similar to those shown in Figs. 2b and 2c, respectively, can be obtained by averaging the SST anomalies along the mean path of the western and eastern OE fronts. To expound on this point, we regress the observed SST anomaly field against the low-pass-filtered PCs of the EOF mode 1 in the western and eastern OE regions, respectively. Figure 4a shows the resultant SST map regressed to the OE-west PC time series. It reveals locally enhanced warm SST anomalies appearing along the east coast of Japan and north of the KE's quasi-stationary meanders. Along the KE path, the regressed SST values are negative and this is consistent with the conceptual scenario put forth in the preceding section; namely, when the upstream KE is in its unstable phase, the eastward-flowing KE jet is weakened and warm (cold) SST anomalies are generated north (south) of the KE due to enhanced cross-frontal eddy heat transport. Plotting out the SST anomalies

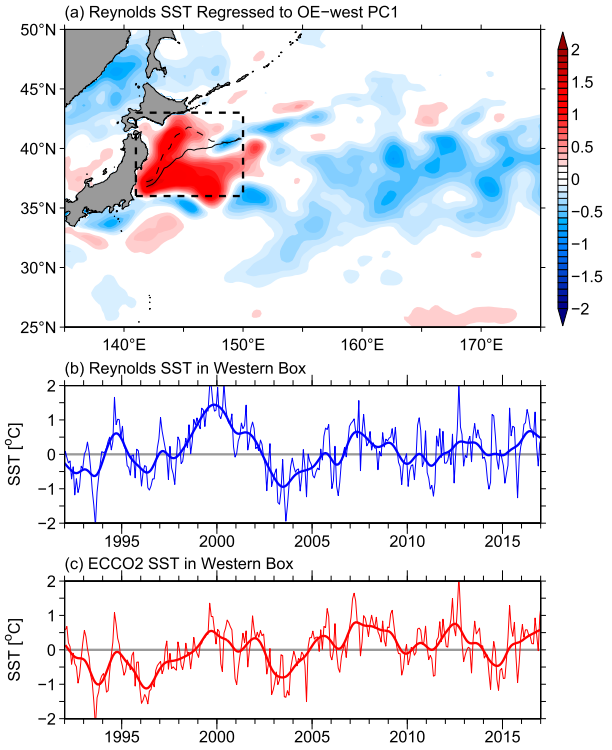

FIG. 4. (a) Distribution of the observed SST anomalies (1981–2016) regressed to the EOF mode-1 PC of the western OE region (i.e., Fig. 2b). (b) The observed SST time series in the OE-west area delineated by the thick dashed lines in (a). (c) The ECCO2-derived SST time series in the OE-west box. Thin solid and dashed lines in (a) denote the mean and shift of the western OE front identified in Fig. 2a.

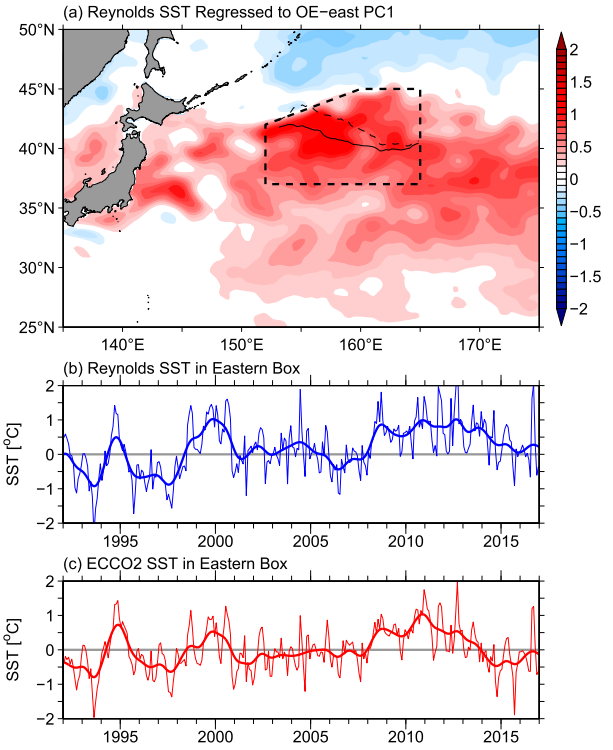

FIG. 5. (a) Distribution of the observed SST anomalies (1981–2016) regressed to the EOF mode-1 PC of the eastern OE region (i.e., Fig. 2c). (b) The observed SST time series in the OE-east area delineated by the thick dashed lines in (a). (c) The ECCO2-derived SST time series in the OE-east box. Thin solid and dashed lines in (a) denote the mean and shift of the eastern OE front identified in Fig. 2a.

in the box 36°–43°N, 141°–150°E (see Fig. 4b and the dashed box in Fig. 4a) indicates that the dominant OE-west variability as encapsulated by the mode-1 PC (i.e., Fig. 2b) can be favorably described by the SST changes in this representative box.[3]

Figure 5a shows the corresponding SST map regressed to the mode-1 PC of the OE variability east of 153°E. Not surprisingly, the maximum SST anomalies in this case are confined to the region along and south of OE-east. Similar to the results presented for the OE-west variability, plotting out the SST anomaly time series in the representative box indicated by the dashed line in Fig. 5a reveals that it also exhibits a good correlation with the mode-1 PC for the OE-east variability ($r = 0.72$ between Figs. 5b and 2c).

The results shown in Figs. 4 and 5 suggest an exploration of regional temperature variations can shed light on the OE-west and OE-east variability as described above from the EOF analysis. To pursue this, we follow many previous studies (e.g., Qiu 2000; Vivier et al. 2002; Tomita et al. 2002; Kwon and Deser 2007; Pak et al. 2017) and conduct an upper-ocean temperature budget analysis in the broad region of the western North Pacific Ocean. The governing equation for the upper-ocean temperature can be written as follows:

$$\frac{\partial T}{\partial t} = -\mathbf{u}\cdot\nabla T + \frac{1}{\rho C_p}\frac{\partial q}{\partial z} + K_h\nabla_h^2 T + \frac{\partial}{\partial z}\left(K_z\frac{\partial T}{\partial z}\right), \qquad (1)$$

where $\mathbf{u} = (u, v, w)$ is the three-dimensional velocity vector, ∇ is the three-dimensional gradient operator, q is the heat flux, ρ is the reference seawater density, C_p is the specific heat of seawater, ∇_h^2 is the horizontal Laplacian operator, and K_h and K_z are the horizontal and vertical eddy diffusivity, respectively. To quantify the upper-ocean temperature changes, we use the output of the ECCO2 state estimate, which, as we noted in section 2, is thermodynamically consistent [hence the validity of Eq. (1)]. Notice that the ECCO2 state estimate produces reasonably good thermal structures in the upper

[3] The correlation coefficient between the time series in Figs. 2b and 4b is $r = 0.63$. Although a higher r value can be achieved by choosing the "box" for SST anomalies more elaboratively, this is not pursued here because our subsequent temperature budget analysis is largely independent of the chosen box.

ocean of our interest.[4] For example, Figs. 4c and 5c show the ECCO2 SST anomalies in the two boxes relevant for the OE-west and OE-east variability, respectively. By comparing to their observed time series shown in Figs. 4b and 5b, it is clear that the ECCO2 output captures the low-frequency SST changes, as well as many of the intraseasonal SST anomalies. The correlation coefficients between the ECCO2 and observed SST time series are $r = 0.64$ and $r = 0.82$ in the OE-west and OE-east boxes, respectively.

To evaluate the relative importance of various processes contributing to the SST changes, it is useful to integrate Eq. (1) from sea surface down to a fixed depth H that is deeper than the winter mixed layer and then divide by H:

$$\frac{\partial}{\partial t}\left(\frac{1}{H}\int_{-H}^{0} T\,dz\right) = -\frac{1}{H}\int_{-H}^{0} \mathbf{u}\cdot\nabla T\,dz + \frac{Q_{\text{net}}}{\rho C_p H} + \left(\frac{K_h}{H}\int_{-H}^{0}\nabla_h^2 T\,dz - \frac{K_z}{H}\frac{\partial T}{\partial z}\bigg|_{z=-H}\right), \tag{2}$$

where Q_{net} denotes the net surface heat flux. Physically, the LHS of Eq. (2) indicates the time rate of change of averaged temperature in the upper ocean, the first term on the RHS is the advective temperature flux convergence through the upper-ocean water column, the second term on the RHS is the net heat exchange through the sea surface, and the last term in parentheses is the diffusive temperature flux convergence due to subgrid-scale perturbations in the ECCO2 model. In the OE region of our interest, the deepest winter mixed layer depth ranges from 200 to 240 m, and, as such, $H = 250$ m is adopted in our analysis below. For brevity, $T_{250\text{m}} = \int_{-H}^{0} T\,dz/H$ will be used to denote the upper-ocean temperature signals. In the OE-west and OE-east boxes of our interest, the ECCO2 $T_{250\text{m}}$ and SST anomaly time series have a correlation at 0.77 and 0.72, respectively, and both of these coefficients are significant at the 95% confidence level. Since the diffusive temperature flux convergence cannot be accurately evaluated from the available 3-day ECCO2 product, the last term in Eq. (2) will be calculated as the residue of the three other terms in our following budget analysis.

[4] In addition to its reproducibility of upper-ocean temperature signals, a recent study of ours (Yang et al. 2017, their Fig. 4) has revealed that the ECCO2 state estimate is capable of reproducing the mean advection and time-varying mesoscale eddy modulations in the KE region when compared to the AVISO product.

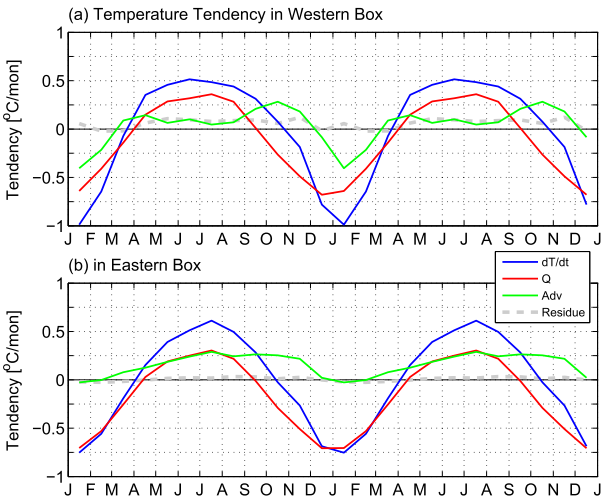

FIG. 6. Climatological upper-ocean temperature tendency budget time series (°C month^{-1}) in (a) the OE-west and (b) the OE-east boxes. For clarity, the annual cycle is repeated twice.

Figures 6a and 6b compare the climatological upper-ocean temperature budget as a function of calendar months in the OE-west and OE-east boxes, respectively. On the seasonal time scale, it is known that the rate of change of upper-ocean temperature in the KE and OE regions is largely balanced by the surface net heat flux forcing and that the temperature advection plays a secondary role (e.g., Qiu and Kelly 1993; Vivier et al. 2002). The ECCO2 results shown in Fig. 6 clearly confirm these notions. One subtle, but illuminating, point revealed in Fig. 6 is that while the seasonal net heat flux forcing is similar in amplitude in the two OE boxes, the seasonal amplitude for rate of temperature change is larger in the western than the eastern box owing to the advective flux convergence (i.e., 0.65° vs 0.25°C month^{-1}). Specifically, in the OE-west box, cold advection convergence occurs in DJF as a result of the seasonally intensified Oyashio along the coast of Japan (e.g., Qiu 2002; Ito et al. 2004). In the OE-east box where upper-ocean waters are supplied from the crests of the KE quasi-stationary meanders (e.g., Isoguchi et al. 2006; Wagawa et al. 2014), climatological advection always works to warm OE-east.

To explore the low-frequency upper-ocean temperature changes, it is more convenient to examine the temperature budget by removing the seasonal cycle and integrating Eq. (2) in time. With time integration, the LHS of Eq. (2) gives us now the time-varying $T_{250\text{m}}$ that is of our direct interest. Before delving into the local temperature budget in the OE boxes, it is beneficial to first have a look at the results in the broad western North Pacific Ocean. Figures 7a–c show the correlation coefficient maps between the time series of $T_{250\text{m}}$ and the time-integrated surface heat flux forcing, the

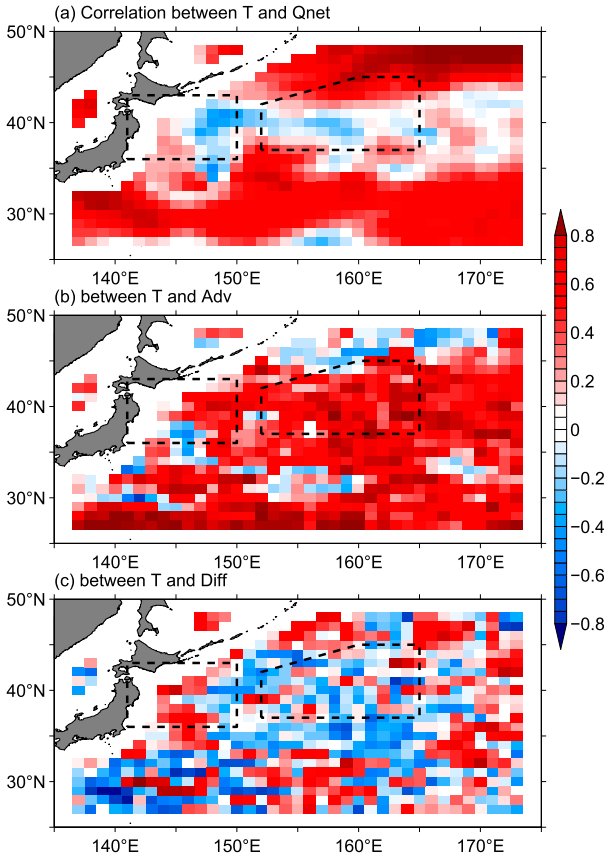

FIG. 7. Correlation coefficient maps between the upper-ocean temperature T_{250m} and (a) time-integrated Q_{net} forcing, (b) time-integrated advective flux convergence, and (c) time-integrated diffusive flux convergence. Correlation values are averaged in overlapping 4° × 4° boxes, and areas adjacent to land are blanked out. Dashed areas indicate the OE-west and OE-east regions also defined in Figs. 4a and 5a, respectively.

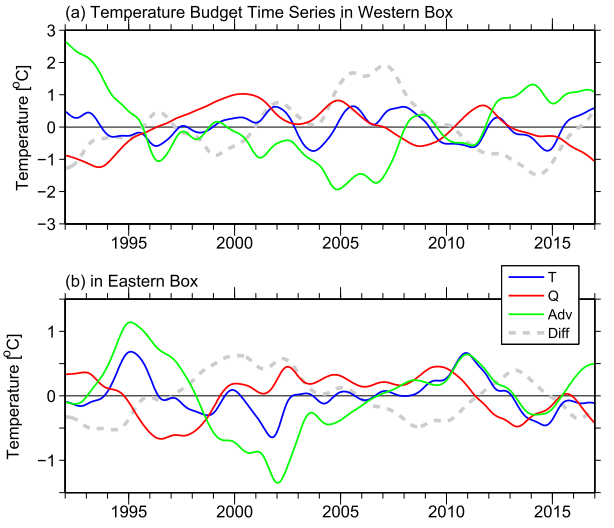

FIG. 8. Time series of time-integrated upper-ocean temperature budget equations in (a) OE-west box and (b) OE-east box. Blue lines denote T_{250m}, red lines denote the time-integrated Q_{net} forcing, green lines denote the time-integrated advective flux convergence, and gray dashed lines denote the time-integrated diffusive flux convergence.

time-integrated advective flux convergence, and the time-integrated diffusive flux convergence, respectively. For the surface heat flux forcing, Fig. 7a reveals a clear spatially coherent pattern with negative correlation values appearing in the regions north of the KE and along the path of the OE fronts. Physically, this implies that rather than being forced by the surface net heat fluxes, the time-varying T_{250m} acts as a driver determining the local surface heat flux anomalies. Notice that this result based on the ECCO2 state estimate is consistent with the previous analysis on the SST and surface heat flux relationship by Tanimoto et al. (2003). Outside of the OE and its confluence region with the KE, the correlation in Fig. 7a is by and large positive, indicating the importance of surface heat flux forcing in driving, at least partially, the low-frequency changes in T_{250m}.

In contrast to the surface heat flux forcing, Fig. 7b reveals that the advective flux convergence in broad regions correlates positively with T_{250m}, and this is particularly true in the KE, OE, and their confluence regions. That advection plays an important role in driving the low-frequency upper-ocean temperature changes in the OE and KE regions is in agreement with many previous analysis results (e.g., Qiu 2000; Vivier et al. 2002; Tomita et al. 2002; Kwon and Deser 2007; Pak et al. 2017). Notice that north of 45°N in the western subarctic gyre, T_{250m} changes are no longer controlled by the advective flux convergence forcing. Instead, surface heat fluxes merge as the dominant forcing agent.

In Fig. 7c, we plot the correlation between T_{250m} and the time-integrated diffusive flux convergence forcing [evaluated from the residue of the three other terms in Eq. (2)]. By and large, the correlation value appears small or negative, indicating the diffusive heat flux convergence works in general to damp the temperature anomalies generated by the surface heat flux and advective flux convergence forcings. That the diffusive flux convergence term acts to reduce the effect of the two other forcing terms on the RHS of Eq. (2) is also discernible in Fig. 8, in which we plot the time series of the time-integrated temperature budget terms averaged in the OE-west and OE-east boxes, respectively. Compared to the T_{250m} signals in both boxes (blue lines), the advective flux convergence forcing and, to a lesser extent, the surface heat flux forcing tend to have large amplitudes, and the diffusive flux convergence term (gray dashed lines) acts in many clear instances in Fig. 8 to compensate for these large forcing terms. The linear

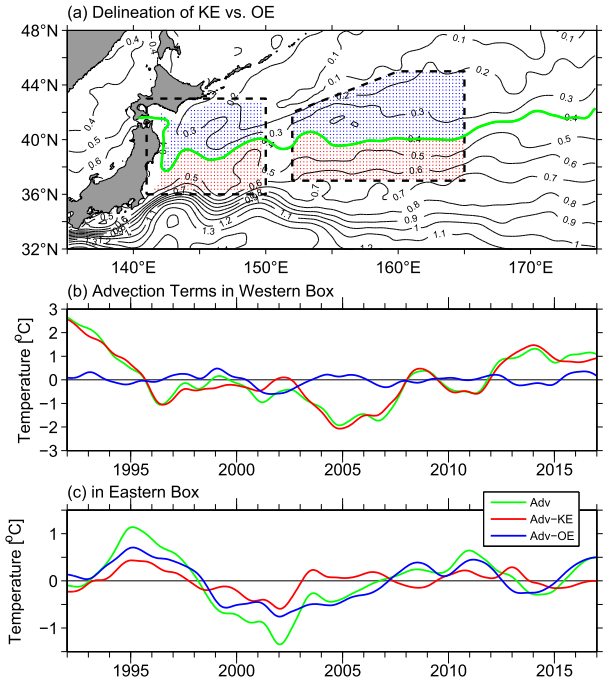

FIG. 9. (a) Mean SSH field (m) based on Rio et al. (2011). The green contour denotes the 0.4-m SSH isoline, and it provides a time-mean boundary between the surface subtropical vs subarctic circulation. Time-integrated advective flux convergence in (b) the OE-west and (c) the OE-east box. Green lines in (b) and (c) denote the total advective flux convergence from the KE and OE areas delineated in (a), and red and blue lines denote the advective flux convergence from the KE and OE areas separately.

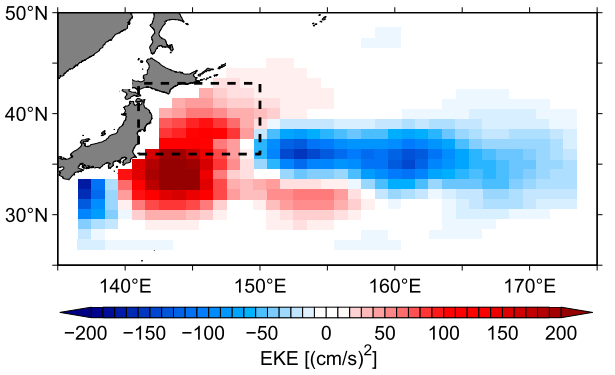

FIG. 10. Regression map of AVISO-derived EKE onto the EOF mode-1 PC (i.e., Fig. 2b) from the OE-west region. Dashed area denotes that of OE-west.

correlation coefficients between the gray dashed line and sum of the green and red lines in Figs. 8a,b are both −0.88. Consistent with the results presented in Fig. 7, Fig. 8 reveals that rather than the surface heat flux forcing, it is the oceanic processes [i.e., the advective flux convergence (or its sum with the diffusive flux convergence)] that are responsible for the low-frequency T_{250m} changes in the OE-west and OE-east regions.

5. Discussion

The upper-ocean temperature budget analyses above point to the importance of advection in controlling the T_{250m} changes in both the OE-west and OE-east regions. To further clarify the processes underlying the advective flux convergence and relate them to the KE variability, we divide the OE-west and OE-east boxes into two parts. The green curve in Fig. 9a denotes the 0.4-m mean SSH isoline derived by Rio et al. (2011). Since the SSH isolines are equivalent geostrophic streamlines, it is clear from Fig. 9a that this green line serves as a reasonable boundary separating the northern area under the OE influence from the southern area under the KE influence. Not coincidentally, the green curve follows roughly the time-mean OE fronts depicted in Fig. 2a. Based on this dividing line, we separate the advective flux convergence forcing in the OE-west box (green line in Fig. 9b) into its OE versus KE contributions (blue and red lines in Fig. 9b, respectively). Despite the areal coverage by the OE and KE influence being about the same, the total advective flux convergence in the OE-west box is nearly exclusively determined by that under the southern KE influence. In contrast, Fig. 9c reveals that the advective flux convergence in the OE-east box has approximately equal contributions from the OE- and KE-influenced areas.

To gain a better insight into this difference between the OE-west and OE-east boxes, it is instructive to examine the advective processes in further detail. In section 3, we noted that the dominant OE-west variability was possibly related to the upstream KE pathlength variations and hinted at the roles played by the mesoscale eddy modulations. To expound on this hypothesis, we plot in Fig. 10 the regression map of the time series of AVISO-derived surface eddy kinetic energy (EKE), given by

$$\mathrm{EKE} = \frac{1}{2}(u_g'^2 + v_g'^2) = \frac{1}{2}\left[\left(-\frac{g}{f}\frac{\partial h'}{\partial y}\right)^2 + \left(\frac{g}{f}\frac{\partial h'}{\partial x}\right)^2\right], \quad (3)$$

onto the OE-west mode-1 PC, where f is the Coriolis parameter, g the gravitational constant, and h' the SSH anomaly from AVISO, respectively. The highest regression value in Fig. 10 is detected in the upstream KE region, and a positive regression band with progressively decreasing amplitude is found to spread northward off the east coast of Japan. This regression pattern supports the hypothesis put forth in section 3 and the

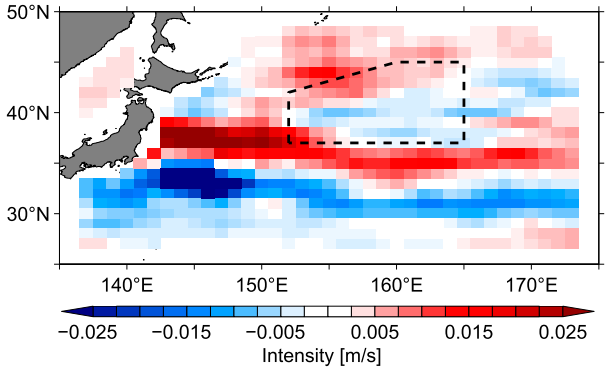

FIG. 11. Regression map of AVISO-derived circulation intensity onto the EOF mode-1 PC (i.e., Fig. 2c) from the OE-east region. Dashed area denotes that of OE-east.

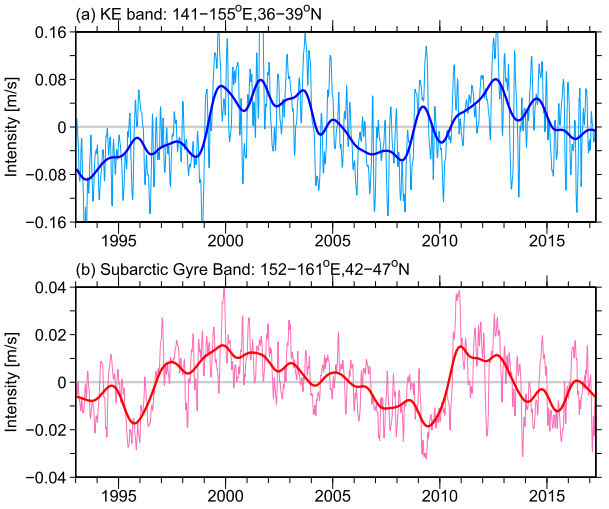

FIG. 12. Time series of the AVISO-derived circulation intensity changes in the band (a) north of the KE (36°–39°N, 141°–155°E) and (b) north of the OE-east (42°–47°N, 152°–161°E).

advective flux convergence analysis result of Fig. 9b; namely, 1) the OE-west variability is primarily induced by the advective flux convergence in the southern KE area, and 2) the source responsible for the time-varying advection is the mesoscale eddy modulations associated with the KE dynamical state.

With respect to the dominant OE variability east of 153°E, we noted in section 3 that the OE-east mode-1 PC had a favorable correlation with the mean position changes of the KE jet from 140° to 165°E. To relate this result to the advective flux convergence analysis shown in Fig. 9c, we plot in Fig. 11 the regression map of the time series of the AVISO-derived surface circulation intensity changes, given by

$$I = \mathbf{u}'_g \cdot \frac{\overline{\mathbf{u}}_g}{|\overline{\mathbf{u}}_g|}, \tag{4}$$

onto the OE-east mode-1 PC, where $\mathbf{u}'_g = (u'_g, v'_g)$ is the time-varying surface geostrophic flow vector and $\overline{\mathbf{u}}_g$, its time-mean vector from Rio et al. (2011). A positive I in Eq. (4) indicates a strengthened surface flow projected to the time-mean surface circulation. Unlike the regression map of Fig. 10, two high positive regression bands exist in Fig. 11 surrounding the OE-east box: one band appears along the northern edge of the KE jet along 36°–39°N east of Japan. Since the regression values immediately south of this band are negative, this suggests that the OE-east variability is in part associated with the coherent meridional shift of the KE jet from 140° to beyond 160°E. While coherent in its zonal extent, the regression map in Fig. 11 reveals that it is the upstream KE position fluctuations west of 153°E that are most effective in generating the OE-east advective flux convergence changes shown by the red line in Fig. 9c. Indeed, plotting out the time series of I averaged in the area of 36°–39°N, 141°–155°E (Fig. 12a) reveals that it is closely related to the zonal-mean KE position changes shown in Fig. 3b (the two time series have a correlation coefficient $r = 0.75$). A northward shift by the KE jet works to carry warmer subtropical-origin water into the OE-east box, intensifying the OE front east of 153°E.

The other high positive regression band in Fig. 11 exists in the northern periphery of the OE-east box. Despite residing inside the western subarctic gyre, the upper-ocean circulation changes averaged in this peripheral area north of OE-east (i.e., 42°–47°N, 152°–161°E) exhibit decadal fluctuations similar to the KE position changes in the subtropical gyre (cf. Figs. 12a and 12b). Geographically, this high regression peripheral area corresponds favorably with the OE front dubbed J1 by Isoguchi et al. (2006, their Fig. 11b) and quasi-stationary jet (QSJ) by Wagawa et al. (2014). In both of these studies, the authors have found that low-frequency J1 or QSJ variability is correlated to the upstream KE position changes, a result consistent with our findings in Fig. 12.

To clarify the causes responsible for the circulation changes north of OE-east, we plot in Fig. 13 the SSH anomaly field regressed to the time series of Fig. 12b at different lead times. At zero lead time, Fig. 13a reveals the northeast–southwest-tilted SSH anomaly patterns that are characteristic of the wind-forced SSH changes via latitude-dependent Rossby wave adjustment (e.g., Qiu 2003). Inside the northern OE-east periphery denoted by the dashed box, the SSH anomalies are positive and negative in the southeast and northwest corners, respectively, reflecting the enhanced upper-ocean circulation along OE-east. As the lead time increases from 1 to 4 yr, it can be seen in Figs. 13b–e that both the

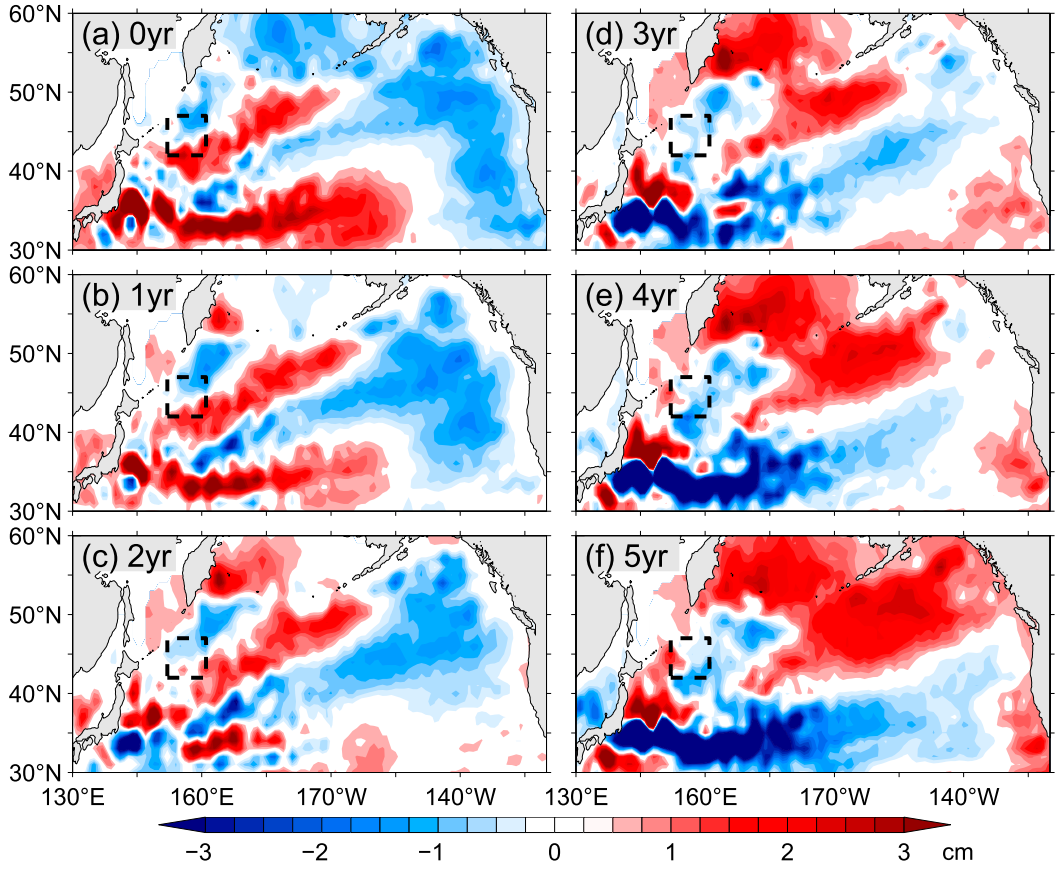

FIG. 13. SSH anomaly maps regressed to the time series of AVISO-derived circulation intensity changes in the northern periphery of the OE-east box (Fig. 12b) at different lead times: (a) 0, (b) 1, (c) 2, (d) 3, (e) 4, and (f) 5 yr. Dashed lines denote the northern periphery area within which the circulation intensity time series is calculated.

positive and negative SSH anomalies in the dashed box in Fig. 13a shift progressively eastward. The positive SSH anomaly, for example, is located near the date line when the lead time is 4 yr, indicating that the westward-propagating speed in the 42°–47°N band is about $0.015\,\mathrm{m\,s^{-1}}$. This speed agrees with the long baroclinic Rossby wave phase velocity detected previously for the western subarctic gyre (e.g., Qiu 2003, his Fig. 7). At the lead time of 5 yr, Fig. 13f exhibits a broadscale SSH anomaly pattern that is nearly identical, but with reversed signs, to that shown in Fig. 13a. The regression results shown in Fig. 13 clearly highlight the dominance of the decadal wind-forced SSH fluctuations and their adjustment through baroclinic Rossby waves in the North Pacific basin.

It is relevant to ask why the two processes contributing to the OE-east variability, one being part of the subtropical circulation and the other part of the subarctic circulation, should have in-phase decadal fluctuations as identified in Fig. 12. To answer this question, it is important to emphasize that the upper-ocean circulation variability related to the KE position changes (Figs. 12a or 3b) is caused by the wind-forced SSH anomalies in the KE's southern recirculation gyre band of 32°–34°N (e.g., Qiu and Chen 2005). Along this latitude, baroclinic Rossby wave speed is $0.038\,\mathrm{m\,s^{-1}}$ (Fig. 7 in Qiu 2003), more than twice that along the 42°–47°N band relevant for the SSH anomalies in the northern periphery of OE-east. As demonstrated in Figs. 13a,f, SSH anomalies forced by the decadal storm-track variability are commonly initiated around 160°W in the eastern North Pacific basin and tend to have opposite signs north and south of 40°N (Di Lorenzo et al. 2008). Along 32°–34°N for the KE southern recirculation gyre, it takes $T = 5074\,\mathrm{km}\ (0.038\,\mathrm{m\,s^{-1}})^{-1} = 4.2\,\mathrm{yr}$ for the wind-induced SSH anomalies at 160°W to reach 155°E; along 42°–47°N just north of OE-east, this transit time increases to $T = 4315\,\mathrm{km}\ (0.015\,\mathrm{m\,s^{-1}})^{-1} = 9.1\,\mathrm{yr}$. It is this slower adjustment of the SSH anomalies along the northern OE-east periphery by about half of a decadal cycle that causes the in-phase contributions to OE-east by the two processes shown in Fig. 12.

Finally, we comment on the lack of contemporaneous correlation between the leading EOF mode-1 PCs in the OE-west and OE-east regions. Dynamically, this is related to the lack of contemporaneous correlation between the level of eddy variability in the upstream KE and the position changes of the KE (recall Figs. 3a,b). While the decadal KE variability is known to be generated by wind stress curl forcing across the North Pacific basin, manifestation of this variability has subtle phase lags among different properties of the KE system. When the wind-forced, positive SSH anomalies propagate into the KE along 32°–34°N, they work to strengthen the southern recirculation gyre, driving the KE position northward. As detailed in Qiu and Chen (2010, their Fig. 7), this allows the deep-reaching KE jet to flow past a deep passage north of the Shatsky Rise and reduces the mesoscale perturbations generated by KE's interaction with the Shatsky Rise. With an adjustment delay, this brings about the stability in the upstream KE jet. When the wind-forced, negative SSH anomalies propagate into the KE, on the other hand, the southern recirculation gyre is weakened and the KE position retreats southward. This forces the KE jet to flow over the shallow Shatsky Rise near 159°E, generating mesoscale perturbations that destabilize the upstream KE with delay. The time series in Fig. 3 reveals that the observed delay is about 2.5 yr, or a quarter of the decadal cycle, and it is this phase delay between the KE's position and eddy energy level changes that is the cause behind the lack of contemporaneous correlation between the decadal OE variability east versus west of 153°E.

6. Summary

The observed decadal variability in the Kuroshio and Oyashio Extensions has multifaceted manifestations. Rather than exploring them individually, the objectives of our present study are to explore the various aspects of the OE and KE variations in a dynamically interlinked way. A significant amount of the decadal OE and KE variations detected in the past three decades are initiated by large-scale wind stress curl forcing that has its action center over the midlatitude eastern North Pacific. In the past three decades, this remote wind stress curl forcing has a predominant decadal time scale and tends to generate oppositely signed SSH anomalies north and south of 40°N in the eastern North Pacific basin. After propagating westward and passing 165°E, these wind-forced, dipolar SSH anomalies generate responses of the KE and OE in a connected and reinforcing way.

The KE and OE responses when the wind-forced SSH anomalies are positive south, and negative north, of 40°N in the eastern North Pacific can be summarized as follows (the opposite responses are generated when the wind-forced SSH anomaly signs reverse). Following a 4-yr westward propagation, the positive SSH anomalies south of 40°N reach the KE and modify it by strengthening its southern recirculation gyre and shifting its axis northward. In this northerly shifted position, the KE jet is enabled to traverse the prominent Shatsky Rise through a deep passage, reducing the topographically induced eddy perturbations near 159°E. With an adjustment delay of approximately 2.5 yr, the reduced eddy perturbations lower the eddy variability level in the upstream KE region of 141°–153°E. These KE changes impact the neighboring OE in two distinct ways. First, the stabilized upstream KE jet transports less warm waters poleward, and this works to weaken the western OE front existing immediately east of Japan. The northerly shifted KE jet, on the other hand, enhances warm water advection into the OE-east region and contributes to the enhancement of the eastern OE front in between 153° and 165°E. It is important to emphasize that this KE-induced enhancement of the eastern OE front is reinforced by the arrival of westward-propagating positive SSH anomalies induced by the wind stress curl forcing north of 40°N that existed half of a decadal cycle ago. Physically, this reinforcement occurs because the SSH anomalies have a slower propagation speed along the OE latitude and it takes about nine years, or half of a decadal cycle longer, to reach the OE-east region.

The interlinked OE and KE variations identified in this study have important implications. As a result of the 2.5-yr adjustment delay in the changes of the upstream KE eddy variability behind those of the KE position, the decadal eastern and western OE front variability exhibits little contemporaneous correlations. This points to the need to separate the two OE fronts in describing and understanding the long-term OE variations. With regard to the eastern OE front, its variability identified in our study is consistent with the OE index put forth by FSKA11. In FSKA11 and many other studies reviewed in the introduction, the eastern OE front variability has been shown to play an important role in affecting the large-scale tropospheric circulation across the midlatitude North Pacific basin. In our analyses, we have attributed the OE-east variability to the in-phase reinforcement from the wind-forced KE and OE variations. With the 5-yr time difference between the wind-forced SSH signals reaching the OE-east region along the KE and OE latitudes, the maximum reinforcement occurs if the wind stress curl forcing has a decadal period; in other words, wind forcings with all other periods would result in a suboptimal reinforcement. Given the ocean–atmosphere feedback relating to the OE-east variability, could the

predominance of the decadal wind stress curl forcing in the recent three decades be a consequence of this optimal reinforcement? Of course, the 5-yr time difference between the wind-forced KE and OE responses in the OE-east depends critically on the spatial structure of the basinwide wind forcing. Has the interlinked OE and KE variability changed over the longer time scales relating to the climate regime shifts of the Pacific Ocean (e.g., Minobe 1997; Qiu et al. 2016)? These are some of the outstanding questions regarding the North Pacific climate variability and midlatitude ocean–atmosphere interaction that need to be addressed in future studies.

Acknowledgments. This study benefited from discussions with Bunmei Taguchi and Masami Nonaka. Constructive comments made by three anonymous reviewers have significantly improved an early version of the manuscript. The ECCO2 state estimate output used in this study was accessed from ftp://ecco2.jpl.nasa.gov/, the Reynolds OI SST data from ftp://eclipse.ncdc.noaa.gov/, and the merged satellite altimeter data by the CLS Space Oceanography Division as part of the Environment and Climate EU ENACT project. We acknowledge the support of NSF OCE-0926594 and NASA NNX17AH33G to BQ and SC and U.S. Department of Energy Grants DE-SC0005111 and DE-SC006766 to NS.

REFERENCES

Ceballos, L., E. Di Lorenzo, C. D. Hoyos, N. Schneider, and B. Taguchi, 2009: North Pacific Gyre Oscillation synchronizes climate variability in the eastern and western boundary current systems. *J. Climate*, **22**, 5163–5174, doi:10.1175/2009JCLI2848.1.

Chen, R., G. R. Flierl, and C. Wunsch, 2014: A description of local and nonlocal eddy–mean flow interaction in a global eddy-permitting state estimate. *J. Phys. Oceanogr.*, **44**, 2336–2352, doi:10.1175/JPO-D-14-0009.1.

Di Lorenzo, E., and Coauthors, 2008: North Pacific Gyre Oscillation links ocean climate and ecosystem change. *Geophys. Res. Lett.*, **35**, L08607, doi:10.1029/2007GL032838.

Ducet, N., P.-Y. Le Traon, and G. Reverdin, 2000: Global high-resolution mapping of ocean circulation from TOPEX/Poseidon and ERS-1 and -2. *J. Geophys. Res.*, **105**, 19 477–19 498, doi:10.1029/2000JC900063.

Favorite, F., A. J. Dodimead, and K. Nasu, 1976: Oceanography of the subarctic Pacific region, 1960–71. United States Fish and Wildlife Service Rep. FWLB0583, 187 pp., https://catalog.data.gov/dataset/oceanography-of-the-subarctic-pacific-region-1960-71/resource/a3934699-f754-4f4c-967a-5671cdb3f8cb.

Frankignoul, C., N. Sennéchael, Y.-O. Kwon, and M. A. Alexander, 2011: Influence of the meridional shifts of the Kuroshio and the Oyashio Extensions on the atmospheric circulation. *J. Climate*, **24**, 762–777, doi:10.1175/2010JCLI3731.1.

Fu, L.-L., 2009: Pattern and velocity of propagation of the global ocean eddy variability. *J. Geophys. Res.*, **114**, C11017, doi:10.1029/2009JC005349.

Isoguchi, O., H. Kawamura, and E. Oka, 2006: Quasi-stationary jets transporting surface warm waters across the transition zone between the subtropical and the subarctic gyres in the North Pacific. *J. Geophys. Res.*, **111**, C10003, doi:10.1029/2005JC003402.

Ito, S.-I., K. Uehara, T. Miyao, H. Miyake, I. Yasuda, T. Watanabe, and Y. Shimizu, 2004: Characteristics of SSH anomaly based on TOPEX/Poseidon altimetry and in situ measured velocity and transport of Oyashio on OICE. *J. Oceanogr.*, **60**, 425–437, doi:10.1023/B:JOCE.0000038059.54334.6b.

Kawai, H., 1972: Hydrography of the Kuroshio Extension. *Kuroshio—Its Physical Aspect*, H. Stommel and K. Yoshida, Eds., University of Tokyo Press, 235–354.

Kelly, K. A., R. J. Small, R. M. Samelson, B. Qiu, T. M. Joyce, Y.-O. Kwon, and M. F. Cronin, 2010: Western boundary currents and frontal air–sea interaction: Gulf Stream and Kuroshio Extension. *J. Climate*, **23**, 5644–5667, doi:10.1175/2010JCLI3346.1.

Kida, S., and Coauthors, 2015: Oceanic fronts and jets around Japan: A review. *J. Oceanogr.*, **71**, 469–497, doi:10.1007/s10872-015-0283-7.

Kouketsu, S., H. Tomita, E. Oka, S. Hosoda, T. Kobayashi, and K. Sato, 2012: The role of meso-scale eddies in mixed layer deepening and mode water formation in the western North Pacific. *J. Oceanogr.*, **68**, 63–77, doi:10.1007/s10872-011-0049-9.

Kwon, Y.-O., and C. Deser, 2007: North Pacific decadal variability in the Community Climate System Model version 2. *J. Climate*, **20**, 2416–2433, doi:10.1175/JCLI4103.1.

——, and T. M. Joyce, 2013: Northern Hemisphere winter atmospheric transient eddy heat fluxes and the Gulf Stream and Kuroshio–Oyashio Extension variability. *J. Climate*, **26**, 9839–9859, doi:10.1175/JCLI-D-12-00647.1.

——, M. A. Alexander, N. A. Bond, C. Frankignoul, H. Nakamura, B. Qiu, and L. Thompson, 2010: Role of the Gulf Stream and Kuroshio–Oyashio systems in large-scale atmosphere–ocean interaction: A review. *J. Climate*, **23**, 3249–3281, doi:10.1175/2010JCLI3343.1.

Ma, X., and Coauthors, 2016: Western boundary currents regulated by interaction between ocean eddies and the atmosphere. *Nature*, **535**, 533–537, doi:10.1038/nature18640.

Marshall, J. C., A. Adcroft, C. Hill, L. Perelman, and C. Heisey, 1997: A finite-volume, incompressible Navier Stokes model for studies of the ocean on parallel computers. *J. Geophys. Res.*, **102**, 5753–5766, doi:10.1029/96JC02775.

Masunaga, R., H. Nakamura, T. Miyasaka, K. Nishii, and B. Qiu, 2016: Interannual modulations of oceanic imprints on the wintertime atmospheric boundary layer under the changing dynamical regimes of the Kuroshio Extension. *J. Climate*, **29**, 3273–3296, doi:10.1175/JCLI-D-15-0545.1.

Menemenlis, D., I. Fukumori, and T. Lee, 2005: Using Green's functions to calibrate an ocean general circulation model. *Mon. Wea. Rev.*, **133**, 1224–1240, doi:10.1175/MWR2912.1.

Minobe, S., 1997: A 50–70 year climatic oscillation over the North Pacific and North America. *Geophys. Res. Lett.*, **24**, 683–686, doi:10.1029/97GL00504.

Nakamura, H., and A. S. Kazmin, 2003: Decadal changes in the North Pacific oceanic frontal zones as revealed in ship and satellite observations. *J. Geophys. Res.*, **108**, 3078, doi:10.1029/1999JC000085.

——, T. Sampe, Y. Tanimoto, and A. Shimpo, 2004: Observed associations among storm tracks, jet streams and midlatitude oceanic fronts. *Earth's Climate: The Ocean–Atmosphere*

Interaction, C. Wang, S. P. Xie, and J. A. Carton, Eds., Amer. Geophys. Union, 329–346.

——, ——, A. Goto, W. Ohfuchi, and S.-P. Xie, 2008: On the importance of midlatitude oceanic frontal zones for the mean state and dominant variability in the tropospheric circulation. *Geophys. Res. Lett.*, **35**, L15709, doi:10.1029/2008GL034010.

Nonaka, M., H. Nakamura, Y. Tanimoto, T. Kagimoto, and H. Sasaki, 2006: Decadal variability in the Kuroshio–Oyashio Extension simulated in an eddy-resolving OGCM. *J. Climate*, **19**, 1970–1989, doi:10.1175/JCLI3793.1.

——, ——, ——, ——, and ——, 2008: Interannual-to-decadal variability in the Oyashio and its influence on temperature in the subarctic frontal zone: An eddy-resolving OGCM simulation. *J. Climate*, **21**, 6283–6303, doi:10.1175/2008JCLI2294.1.

Oka, E., B. Qiu, S. Kouketsu, K. Uehara, and T. Suga, 2012: Decadal seesaw of the Central and Subtropical Mode Water formation associated with the Kuroshio Extension variability. *J. Oceanogr.*, **68**, 355–360, doi:10.1007/s10872-011-0098-0.

O'Reilly, C. H., and A. Czaja, 2015: The response of the Pacific storm track and atmospheric circulation to Kuroshio Extension variability. *Quart. J. Roy. Meteor. Soc.*, **141**, 52–66, doi:10.1002/qj.2334.

Pak, G., Y. H. Park, F. Vivier, R. Bourdallé-Badie, G. Garric, and K.-I. Chang, 2017: Upper-ocean thermal variability controlled by ocean dynamics in the Kuroshio-Oyashio Extension region. *J. Geophys. Res. Oceans*, **122**, 1154–1176, doi:10.1002/2016JC012076.

Qiu, B., 2000: Interannual variability of the Kuroshio Extension system and its impact on the wintertime SST field. *J. Phys. Oceanogr.*, **30**, 1486–1502, doi:10.1175/1520-0485(2000)030<1486:IVOTKE>2.0.CO;2.

——, 2001: Kuroshio and Oyashio currents. *Encyclopedia of Ocean Sciences*, K. Turekian, S. A. Thorpe, and J. Steele, Eds., Academic Press, 1413–1425.

——, 2002: Large-scale variability in the midlatitude subtropical and subpolar North Pacific Ocean: Observations and causes. *J. Phys. Oceanogr.*, **32**, 353–375, doi:10.1175/1520-0485(2002)032<0353:LSVITM>2.0.CO;2.

——, 2003: Kuroshio Extension variability and forcing of the Pacific decadal oscillations: Responses and potential feedback. *J. Phys. Oceanogr.*, **33**, 2465–2482, doi:10.1175/2459.1.

——, and K. A. Kelly, 1993: Upper ocean heat balance in the Kuroshio Extension region. *J. Phys. Oceanogr.*, **23**, 2027–2041, doi:10.1175/1520-0485(1993)023<2027:UOHBIT>2.0.CO;2.

——, and S. Chen, 2005: Variability of the Kuroshio Extension jet, recirculation gyre, and mesoscale eddies on decadal time scales. *J. Phys. Oceanogr.*, **35**, 2090–2103, doi:10.1175/JPO2807.1.

——, and ——, 2006: Decadal variability in the formation of the North Pacific Subtropical Mode Water: Oceanic versus atmospheric control. *J. Phys. Oceanogr.*, **36**, 1365–1380, doi:10.1175/JPO2918.1.

——, and ——, 2010: Eddy-mean flow interaction in the decadally modulating Kuroshio Extension system. *Deep-Sea Res. II*, **57**, 1098–1110, doi:10.1016/j.dsr2.2008.11.036.

——, N. Schneider, and S. Chen, 2007: Coupled decadal variability in the North Pacific: An observationally constrained idealized model. *J. Climate*, **20**, 3602–3620, doi:10.1175/JCLI4190.1.

——, S. Chen, and N. Schneider, 2016: Inter-decadal modulations in the dynamical state of the Kuroshio Extension system: 1905-2015. *CLIVAR Exchanges*, No. 69, CLIVAR Project Office, Southampton, United Kingdom, 6–9.

Révelard, A., C. Frankignoul, N. Sennéchael, Y.-O. Kwon, and B. Qiu, 2016: Influence of the decadal variability of the Kuroshio Extension on the atmospheric circulation in the cold season. *J. Climate*, **29**, 2123–2144, doi:10.1175/JCLI-D-15-0511.1.

Reynolds, R. W., T. M. Smith, C. Liu, D. B. Chelton, K. S. Casey, and M. G. Schlax, 2007: Daily high-resolution-blended analyses for sea surface temperature. *J. Climate*, **20**, 5473–5496, doi:10.1175/2007JCLI1824.1.

Rio, M.-H., S. Guinehut, and G. Larnicol, 2011: New CNES-CLS09 global mean dynamic topography computed from the combination of GRACE data, altimetry, and in situ measurements. *J. Geophys. Res.*, **116**, C07018, doi:10.1029/2010JC006505.

Sasaki, Y. N., S. Minobe, and N. Schneider, 2013: Decadal response of the Kuroshio Extension jet to Rossby waves: Observation and thin-jet theory. *J. Phys. Oceanogr.*, **43**, 442–456, doi:10.1175/JPO-D-12-096.1.

Schneider, N., A. J. Miller, and D. W. Pierce, 2002: Anatomy of North Pacific decadal variability. *J. Climate*, **15**, 586–605, doi:10.1175/1520-0442(2002)015<0586:AONPDV>2.0.CO;2.

Seager, R., Y. Kushnir, N. H. Naik, M. A. Cane, and J. Miller, 2001: Wind-driven shifts in the latitude of the Kuroshio–Oyashio Extension and generation of SST anomalies on decadal timescales. *J. Climate*, **14**, 4249–4265, doi:10.1175/1520-0442(2001)014<4249:WDSITL>2.0.CO;2.

Smirnov, D., M. Newman, M. A. Alexander, Y. O. Kwon, and C. Frankignoul, 2015: Investigating the local atmospheric response to a realistic shift in the Oyashio sea surface temperature front. *J. Climate*, **28**, 1126–1147, doi:10.1175/JCLI-D-14-00285.1.

Sugimoto, S., and K. Hanawa, 2009: Decadal and interdecadal variations of the Aleutian low activity and their relation to upper oceanic variations over the North Pacific. *J. Meteor. Soc. Japan*, **87**, 601–614, doi:10.2151/jmsj.87.601.

——, and ——, 2011: Roles of SST anomalies on the wintertime turbulent heat fluxes in the Kuroshio–Oyashio confluence region: Influence of warm eddies detached from the Kuroshio Extension. *J. Climate*, **24**, 6551–6561, doi:10.1175/2011JCLI4023.1.

——, N. Kobayashi, and K. Hanawa, 2014: Quasi-decadal variation in intensity of the western part of the winter subarctic SST front in the western North Pacific: The influence of Kuroshio Extension path state. *J. Climate*, **44**, 2753–2762, doi:10.1175/JPO-D-13-0265.1.

Taguchi, B., S.-P. Xie, N. Schneider, M. Nonaka, H. Sasaki, and Y. Sasai, 2007: Decadal variability of the Kuroshio Extension: Observations and an eddy-resolving model hindcast. *J. Climate*, **20**, 2357–2377, doi:10.1175/JCLI4142.1.

——, H. Nakamura, M. Nonaka, and S. P. Xie, 2009: Influences of the Kuroshio/Oyashio Extensions on air–sea heat exchanges and storm-track activity as revealed in regional atmospheric model simulations for the 2003/04 cold season. *J. Climate*, **22**, 6536–6560, doi:10.1175/2009JCLI2910.1.

——, ——, ——, N. Komori, A. Kuwano-Yoshida, K. Takaya, and A. Goto, 2012: Seasonal evolutions of atmospheric response to decadal SST anomalies in the North Pacific subarctic frontal zone: Observations and a coupled model simulation. *J. Climate*, **25**, 111–139, doi:10.1175/JCLI-D-11-00046.1.

Tanimoto, Y., H. Nakamura, T. Kagimoto, and S. Yamane, 2003: An active role of extratropical sea surface temperature anomalies in determining anomalous turbulent heat flux. *J. Geophys. Res.*, **108**, 3304, doi:10.1029/2002JC001750.

Tomita, T., S.-P. Xie, and M. Nonaka, 2002: Estimates of surface and subsurface forcing for decadal sea surface temperature

variability in the mid-latitude North Pacific. *J. Meteor. Soc. Japan*, **80**, 1289–1300, doi:10.2151/jmsj.80.1289.

Vivier, F., K. A. Kelly, and L. Thompson, 2002: Heat budget in the Kuroshio Extension region: 1993–99. *J. Phys. Oceanogr.*, **32**, 3436–3454, doi:10.1175/1520-0485(2002)032<3436:HBITKE>2.0.CO;2.

Wagawa, T., S.-I. Ito, Y. Shimizu, S. Kakehi, and D. Ambe, 2014: Currents associated with the quasi-stationary jet separated from the Kuroshio Extension. *J. Phys. Oceanogr.*, **44**, 1636–1653, doi:10.1175/JPO-D-12-0192.1.

Wunsch, C., P. Heimbach, R. Ponte, and I. Fukumori, 2009: The global general circulation of the ocean estimated from the ECCO-consortium. *Oceanography*, **22**, 88–103, doi:10.5670/oceanog.2009.41.

Yang, Y., X. S. Liang, B. Qiu, and S. Chen, 2017: On the decadal variability of the eddy kinetic energy in the Kuroshio Extension. *J. Phys. Oceanogr.*, **47**, 1169–1187, doi:10.1175/JPO-D-16-0201.1.

Yasuda, I., 2003: Hydrographic structure and variability in the Kuroshio–Oyashio transition area. *J. Oceanogr.*, **59**, 389–402, doi:10.1023/A:1025580313836.

Yuan, X., and L. D. Talley, 1996: The subarctic frontal zone in the North Pacific: Characteristics of frontal structure from climatological data and synoptic surveys. *J. Geophys. Res.*, **101**, 16 491–16 508, doi:10.1029/96JC01249.